PNAS RESEARCH ARTICLE | CELL BIOLOGY

The amino acid sensor GCN2 controls red blood cell clearance and iron metabolism through regulation of liver macrophages

Phoenix Toboz[a,1], Mehdi Amiri[b,c,1], Negar Tabatabaei[a], Catherine R. Dufour[c], Seung Hyeon Kim[a], Carine Fillebeen[d], Charles E. Ayemoba[a], Arkady Khoutorsky[e], Manfred Nairz[f], Lijian Shao[a], Kostandin V. Pajcini[a], Ki-Wook Kim[a], Vincent Giguère[b,c], Regiana L. Oliveira[g], Marco Constante[h,2], Manuela M. Santos[h], Carlos R. Morales[g], Kostas Pantopoulos[d], Nahum Sonenberg[b,c,3], Sandra Pinho[a,3], and Soroush Tahmasebi[a,3]

Contributed by Nahum Sonenberg; received November 23, 2021; accepted July 20, 2022; reviewed by Jane-Jane Chen and Merav Socolovsky

GCN2 (general control nonderepressible 2) is a serine/threonine-protein kinase that controls messenger RNA translation in response to amino acid availability and ribosome stalling. Here, we show that GCN2 controls erythrocyte clearance and iron recycling during stress. Our data highlight the importance of liver macrophages as the primary cell type mediating these effects. During different stress conditions, such as hemolysis, amino acid deficiency or hypoxia, *GCN2* knockout ($GCN2^{-/-}$) mice displayed resistance to anemia compared with wild-type ($GCN2^{+/+}$) mice. $GCN2^{-/-}$ liver macrophages exhibited defective erythrophagocytosis and lysosome maturation. Molecular analysis of $GCN2^{-/-}$ cells demonstrated that the ATF4-NRF2 pathway is a critical downstream mediator of GCN2 in regulating red blood cell clearance and iron recycling.

mRNA translation | GCN2 | hemolytic stress | RBC | macrophages

Significance

In this study, we define a regulatory pathway controlling tissue-resident macrophages during stress through the translational control of a subset of messenger RNAs (mRNAs) and transcriptional reprogramming. Our data reveal that the GCN2-eIF2α pathway is enriched and activated in macrophages. Using mice devoid of GCN2, we show that lack of GCN2 interferes with the clearance of red blood cells (RBCs) during stress. We report an unexpected role of GCN2 in regulating lysosome maturation and phagocytosis of RBCs by macrophages during stress. Thus, we conclude that GCN2 regulates the clearance of RBCs through translational control of ATF4 mRNA in liver macrophages.

Changes in messenger RNA (mRNA) translation rates are imperative for cells to quickly adjust to internal and environmental stress (1). The integrated stress response (ISR) pathway is a key mechanism that senses different stressors and regulates general and specific mRNA translation to cope with stress. The ISR consists of four stress-sensing kinases known as eukaryotic translation initiation factor 2 alpha kinases (eIF2AKs), including heme-regulated eIF2α kinase (HRI; eIF2AK1), protein kinase R (PKR; eIF2AK2), PKR-like endoplasmic reticulum kinase (PERK; eIF2AK3), and general control nonderepressible 2 kinase (GCN2; eIF2AK4). Each eIF2AK in response to distinct stressors phosphorylates the α subunit of eukaryotic translation initiation factor 2 (eIF2α) (2). eIF2, which consists of three subunits, forms a ternary complex (TC) with methionine-charged initiator transfer RNA (Met-$tRNA_i$) and guanosine triphosphate (GTP). TC joins the small (40S) ribosomal subunit in complex with other translation initiation factors to yield the 43S preinitiation complex, which binds the mRNA to initiate translation (3). Phosphorylation of eIF2α at serine 51 (serine 52 in mouse) converts eIF2 from a substrate to an inhibitor of eIF2B (a guanine nucleotide exchange factor for eIF2 that exchanges guanosine diphosphate (GDP) for GTP), thereby blocking TC formation (4). While the shortage of TC inhibits the translation of most mRNAs, it de-represses the translation of a subset of mRNAs that contain inhibitory upstream open reading frames at their 5′UTRs. This subset of mRNAs encodes key transcription factors such as ATF4 (activating transcription factor 4) (5, 6) that govern how cells respond to various forms of stress (6).

While all four eIF2AKs converge on eIF2 to control translation initiation, each kinase has unique regulatory domains and tissue distribution, which endow them with cell type-specific functions. For instance, PERK plays a critical role in the development and function of pancreatic β cells (7) and myelinating neurons (8). Alternatively, HRI that senses intracellular heme levels and is predominantly expressed in erythroid lineages, plays a critical role in coordinating heme availability with the translation of globin mRNA and in iron-restricted erythropoiesis (9). PKR is ubiquitously expressed in mammalian cells and activated by double-stranded RNA (dsRNA) generated following viral infection (10). GCN2 is the most evolutionary conserved eIF2AK found in all eukaryotes (11). Low levels of amino acids are the best-characterized stressors responsible for the activation of GCN2 (12). Intracellular depletion of amino acids leads to an increase in the level of uncharged tRNA, which activates GCN2 through its binding to histidyl-tRNA synthetase-related domain (12). In addition to amino acid deprivation, several other stressors, such as ultraviolet radiation, viral infection, and proteasome inhibition, can activate GCN2, either through increases in uncharged tRNA or induction of ribosome stalling (13–16). The function of GCN2 has been implicated in physiological and pathological processes, including metabolism, immunity, cancer, and memory formation, through regulation of cell-type-specific functions (17–21).

Author contributions: C.R.D., C.F., K.P., N.S., S.P., and S.T. designed research; P.T., M.A., N.T., C.R.D., S.H.K., C.F., C.E.A., M.N., L.S., K.V.P., K.-W.K., R.L.O., M.C., C.R.M., S.P., and S.T. performed research; M.M.S. and S.T. contributed new reagents/analytic tools; M.A., N.T., C.R.D., S.H.K., C.F., A.K., M.N., L.S., K.V.P. , K.-W.K., V.G., R.L.O., M.C., M.M.S., C.R.M., K.P., N.S., S.P., and S.T. analyzed data; and C.D., A.K., V.G., K.P., N.S., S.P., and S.T. wrote the paper.

Reviewers: J.-J.C., Massachusetts Institute of Technology; and M.S., University of Massachusetts Medical School.

The authors declare no competing interest.

[1]P.T. and M.A. contributed equally to this work.

[2]Present address: Farncombe Family Digestive Health Research Institute, McMaster University, Hamilton, ON, L8S 4K1, Canada.

[3]To whom correspondence may be addressed. Email: sorousht@uic.edu or spinho@uic.edu or nahum.sonenberg@mcgill.ca.

This article contains supporting information online at http://www.pnas.org/lookup/suppl/doi:10.1073/pnas.2121251119/-/DCSupplemental.

Published August 22, 2022.

Several lines of evidence indicate that GCN2 plays a critical role in regulating macrophage (Mφ) function. Abrogation of GCN2 led to increased susceptibility of peritoneal Mφ to infection by dsDNA viruses (20). In a mouse model of inflammatory bowel disease, GCN2-deficient Mφ displayed defective autophagy (18), consistent with studies on the role of GCN2 in autophagosome formation (22). In addition, lack of GCN2 increased Mφ recruitment and production of reactive oxygen species and proinflammatory cytokines in various disease models (22). Mφ play a central role in regulating the balance between production and clearance of red blood cells (RBCs) (23–26). RBCs interact with Mφ at the beginning and end of their life cycle: during RBC production (erythropoiesis) by the erythroblast island Mφ in the bone marrow (BM) (27, 28) and during RBC clearance by the liver and spleen Mφ[26]. The role of Mφ is particularly important for promoting erythropoiesis under stress conditions such as acute blood loss or hemolysis (24–26, 29). In addition to their role in erythropoiesis, Mφ have a concomitant role in the clearance of damaged and senescent RBCs (30, 31). Liver Mφ (Kupffer cells) play an important role in the clearance of RBCs, particularly when the demand for erythrophagocytosis increases because of hemolysis, infection, or hereditary blood diseases (e.g., sickle cell anemia and thalassemia) (26). In this study, we report that GCN2 is expressed in Mφ and that lack of GCN2 impairs Mφ regulation of RBC clearance. Moreover, our data demonstrate that GCN2 through regulation of NRF2 promotes lysosomal function and iron recycling in Mφ. These data uncover a critical role for the amino acid sensor GCN2 in regulating RBC clearance and iron homeostasis upon stress.

Results

GCN2-eIF2α Activity Is Higher in BM Mφ Compared with BM Monocytes and Neutrophils. Given the importance of GCN2 in regulating Mφ functions (20, 22, 32), we assessed the mRNA expression of key components of the GCN2-eIF2α pathway in purified populations of mouse BM mononuclear phagocytes and neutrophils (Fig. 1 *A* and *B*). Reverse transcription-qPCR revealed higher levels of *EIF2AK4* (encoding GCN2) and two well-established transcriptional targets of the ISR pathway, *DDIT3* (DNA damage inducible transcript 3; also known as CHOP) and *PPP1R15A* (protein phosphatase 1 regulatory subunit 15A; also known as GADD34) in Mφ compared with BM neutrophils and $Gr1^{hi}$ or $Gr1^{low}$ monocytes. Relatively high expression of *EIF2AK4* in $Gr1^{low}$ monocytes appears to be compensated by high expression of *EIF2S1* (encoding eIF2α), as evidenced by a lack of downstream target induction. Two other members of the eIF2AK family, *eIF2AK1* and *eIF2AK2*, are also highly expressed in BM Mφ, consistent with their established roles in regulating Mφ in response to different stressors (33) (*SI Appendix*, Fig. S1 *A* and *B*). These data suggest that the GCN2-eIF2α pathway is particularly active in BM Mφ compared with other mononuclear cells.

Lack of GCN2 Impairs RBC Life Cycle during Stress. To study the role of GCN2 in the well-characterized function of Mφ in the maturation and clearance of RBCs (24–26, 34), we used phenylhydrazine (PHZ) treatment (Fig. 1*C*). Our initial analysis at steady state did not detect any significant difference between $GCN2^{+/+}$ and $GCN2^{-/-}$ mice in BM erythropoiesis or in the number of liver, spleen, and BM Mφ. PHZ is an oxidizing hemolytic agent that causes lipid peroxidation of erythrocyte membranes (35) and consequently triggers erythropoiesis (RBC production) and erythrophagocytosis (clearance of damaged RBCs) by tissue-resident Mφ (24, 26). $GCN2^{+/+}$ and $GCN2^{-/-}$ mice developed marked hemolytic anemia 3 d post-PHZ treatment (intraperitoneal [i.p.] injection of 50 mg/kg/d of PHZ for 2 consecutive days, Fig. 1*C* and *SI Appendix*, Table S1). Surprisingly, PHZ-induced anemia was less prominent, and reticulocytosis (a readout for erythropoiesis) was reduced in $GCN2^{-/-}$ mice compared with control $GCN2^{+/+}$ controls (Fig. 1*C*). These data indicate that the higher RBC numbers in $GCN2^{-/-}$ mice are not attributed to excessive erythropoiesis but may stem from a defect in mature RBC clearance. PHZ is a potent oxidizing agent, and intraperitoneal injection of PHZ may have a systemic toxic effect on many tissues. Therefore, to determine whether the difference observed in RBC indices is unique to PHZ-induced hemolytic anemia or can be observed in another model of anemia, we fed $GCN2^{+/+}$ and $GCN2^{-/-}$ mice a leucine-deficient diet (LDD) for 7 d (Fig. 1*D*). Amino acid deficiency is a well-established stressor of GCN2, strongly suppresses hematopoiesis, and induces anemia (36–38). Consistent with the results obtained using PHZ, the LDD-fed $GCN2^{-/-}$ mice maintained higher RBCs, hemoglobin (Hgb), and, hematocrit (Hct) levels. The LDD-fed $GCN2^{-/-}$ mice also exhibited a lower RBC production rate (lower reticulocyte (RT) [%]) compared with LDD-fed $GCN2^{+/+}$ mice (Fig. 1*D*). In response to LDD, $GCN2^{-/-}$ mice displayed lower mean corpuscular volume and lower mean corpuscular Hgb (MCH) compared with $GCN2^{+/+}$ mice (Fig. 1*D*). These data indicate that higher Hgb values in LDD-fed $GCN2^{-/-}$ mice are associated with an increase in RBC numbers rather than elevated MCH. Similarly, under chronic hypoxia (10% O_2; for 9 d), we observed higher RBC, Hgb, and Hct values and lower MCH in $GCN2^{-/-}$ mice compared with $GCN2^{+/+}$ mice (*SI Appendix*, Fig. S1*C*), thus reinforcing the notion that independently of the type of stress, lack of GCN2 impairs RBC life cycle. To confirm that the phenotypes observed in response to PHZ treatment are not restricted to the 129S6/SvEvTac mouse strain, we repeated the PHZ experiment in B6.129S6 genetic background mice and observed similar changes in RBC indices (*SI Appendix*, Fig. S1*D*). Taken together, the data demonstrate that under stress conditions (hemolysis, amino acid deprivation, and hypoxia), GCN2 plays a critical role in regulating RBC life cycle. Since Mφ play a dual role in supporting RBC production and clearance (24–26), high RBC numbers together with low reticulocytes in $GCN2^{-/-}$ mice are consistent with a potential defect in Mφ function.

***GCN2*$^{-/-}$ Mice Produce Fewer RBCs from BM during Hemolysis.** Lower reticulocytosis in PHZ-treated $GCN2^{-/-}$ mice could be attributed to either impaired erythropoiesis or lower erythropoietin (EPO) production secondary to higher Hct values in these mice. Quantitative analysis of BM revealed that during hemolysis, the terminal stage of erythropoiesis (differentiation of orthochromatic erythroblasts to reticulocytes) is less efficient in $GCN2^{-/-}$ mice (Fig. 2 *A* and *B*). In addition, our data identified a significant reduction in proerythroblasts (pro-EB). No significant differences were detected in the spleen size (in both saline and PHZ condition) or extramedullary erythropoiesis between $GCN2^{+/+}$ and $GCN2^{-/-}$ mice (*SI Appendix*, Fig. S2 *A* and *B*). Importantly, the percentage of BM erythroblastic islands was not different between PHZ-treated $GCN2^{+/+}$ and $GCN2^{-/-}$ mice (Fig. 2 *C–E*). Quantification of serum iron, total iron-binding capacity (TIBC), and unsaturated iron-binding capacity (UIBC) revealed no significant difference between PHZ-treated $GCN2^{+/+}$ and $GCN2^{-/-}$ mice (*SI Appendix*, Fig. S1*E*), suggesting that lower RBC production during stress in $GCN2^{-/-}$ mice is not secondary to iron restriction. In response to PHZ, plasma EPO (the

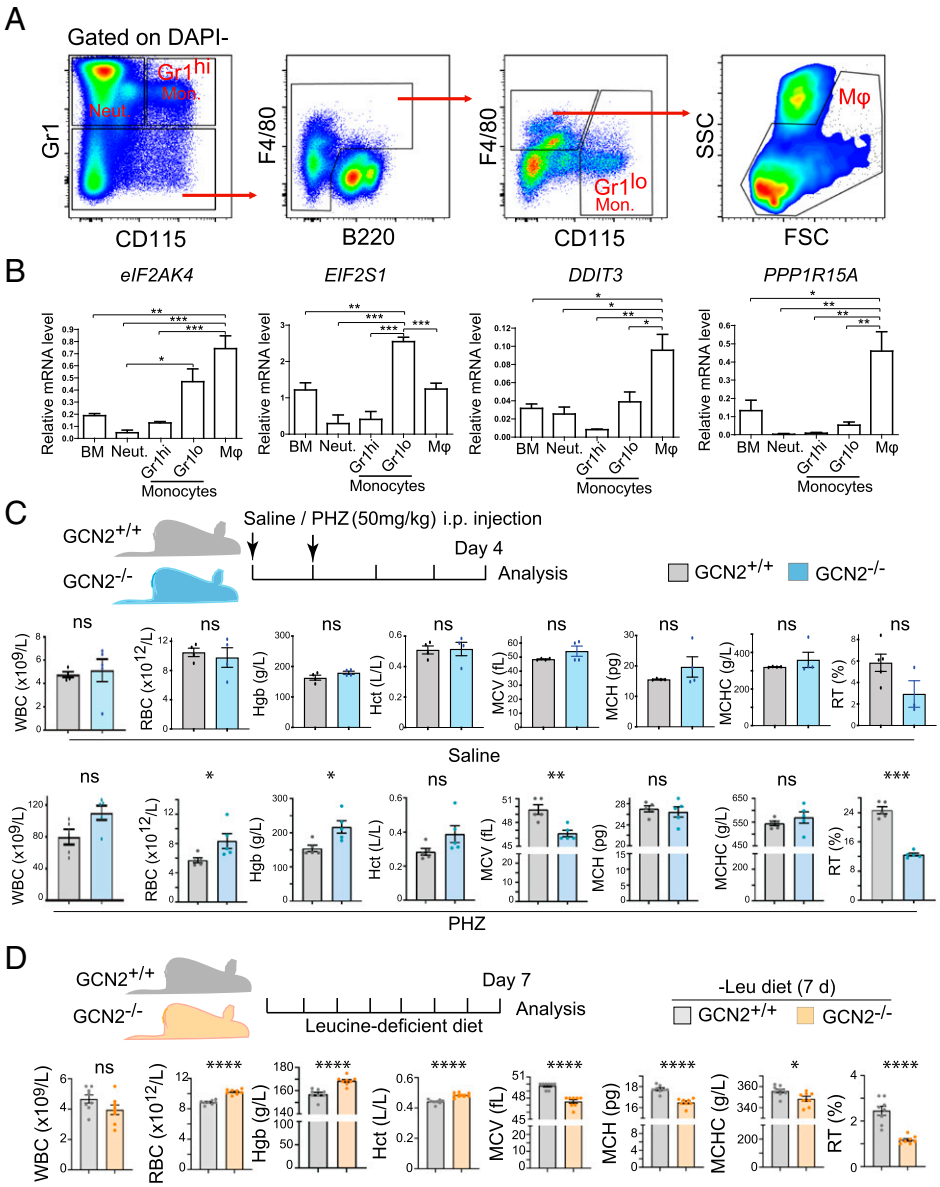

Fig. 1. Lack of GCN2 disrupts RBC life cycle during hemolysis and amino acid deprivation. (*A*) Gating strategy of adult bone marrow (BM) mononucleated cells for each cell population analyzed in panel 1*B* and *SI Appendix*, Fig. S1 *A* and *B*. (*B*) Quantification of mRNA levels of *EIF2AK4* (GCN2), the alpha subunit of eIF2 (*EIF2S1*), and two downstream transcriptional targets of integrated stress response pathway, *DDIT3* and *PPP1R15A*, in total BM, neutrophils (Neut.), Gr1^{hi}, and Gr1^{low} monocytes and macrophages (Mφ). One-way ANOVA. Results are presented as mean ± SEM (n = 3). (*C*) Blood indices of *GCN2*$^{+/+}$ and *GCN2*$^{-/-}$ mice 3 d after i.p. injection of saline or PHZ (50 mg/kg/d) for 2 consecutive days. Two-tailed Student's t test. Results are presented as mean ± SEM (n = 3–5). The full assessment of hematological and serum biochemical indices is summarized in *SI Appendix*, Tables S1 and S2. (*D*) Blood indices of *GCN2*$^{+/+}$ and *GCN2*$^{-/-}$ mice fed a leucine-deficient diet for 7 d. n.s., nonsignificant. Two-tailed Student's t test. Results are presented as mean ± SEM (n = 5,6). *P < 0.05, **P < 0.01, ***P < 0.001, ****P < 0.0001.

primary regulator of RBC production) levels were significantly increased in both *GCN2*$^{+/+}$ and *GCN2*$^{-/-}$ mice; however, there was no significant difference in plasma EPO levels between *GCN2*$^{+/+}$ and *GCN2*$^{-/-}$ mice (Fig. 2*F*). Therefore, our data suggest that higher RBC numbers in the circulation of *GCN2*$^{-/-}$ mice do not impact EPO production, and consequently, erythropoiesis is unaffected by EPO level (39, 40). While the percentage of erythroblastic islands was similar between *GCN2*$^{+/+}$ and *GCN2*$^{-/-}$ mice (Fig. 2*D*), the lack of GCN2 increased the numbers of total BM Mφ and the CD169^{+} "nurse" Mφ subset (Fig. 2*G* and *SI Appendix*, Fig. S1 *F* and *G*). These data suggest a compensatory increase in both BM and CD169^{+} Mφ, which provide a niche for erythropoiesis (24) in *GCN2*$^{-/-}$ mice.

Deletion of GCN2 Impairs Lysosome Maturation and Erythrophagocytosis by Liver Mφ during Hemolysis. The liver is the primary organ where rapid erythrocyte removal occurs during acute hemolysis by the recruitment of F4/80^{high} CD11b^{high} Mφ derived from BM monocytes (26). Fluorescence-activated cell sorting (FACS) analysis revealed that in response to hemolysis, F4/80^{high} CD11b^{high} Mφ derived from BM monocytes were recruited to the liver and spleen (Fig. 3 *A* and *B* and *SI Appendix*, Fig. S2*C*); however, the percentage of recruited Mφ was not significantly different between *GCN2*$^{+/+}$ and *GCN2*$^{-/-}$ mice (Fig. 3*B*). We also did not observe a significant difference in the percentage of liver and spleen Gr1^{hi} neutrophils and monocytes between PHZ-treated *GCN2*$^{+/+}$ and *GCN2*$^{-/-}$ mice (*SI Appendix*, Fig. S2*D*). Liver and spleen Mφ remove damaged RBCs through erythrophagocytosis to release iron, which is either stored in Mφ (bound to ferritin) or released into circulation for another round of erythropoiesis (41). Iron staining using Prussian blue can be used to detect the punctate pattern of iron stores as a surrogate for ferritin-bound iron in Mφ. Strikingly, *GCN2*$^{-/-}$ livers were devoid of a punctate pattern of Prussian blue staining

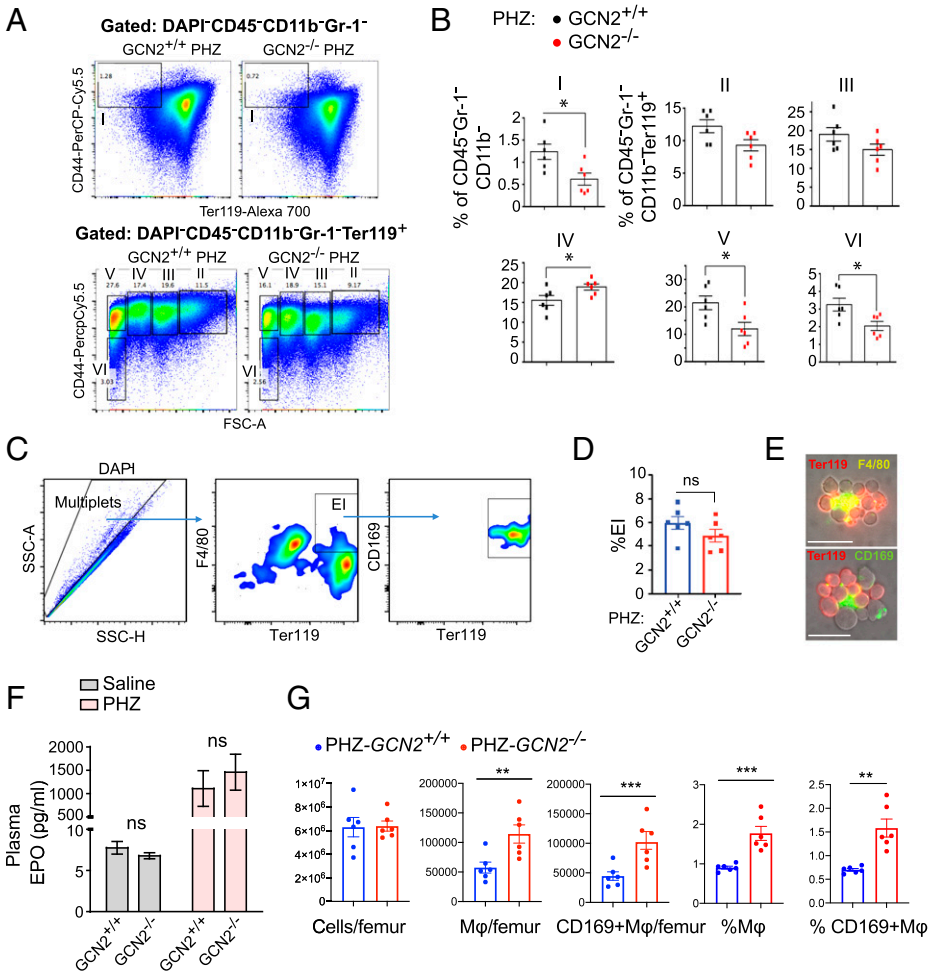

Fig. 2. RBC production is impaired in *GCN2*$^{-/-}$ mice during hemolytic stress. (*A*) FACS plots of gating strategy for quantification of BM erythroblasts presented in panel 2*B*. (*B*) Quantification of BM erythroblasts in response to PHZ injection pro- (I), basophilic (II), polychromatic (III), and orthochromatic (IV) erythroblasts; reticulocytes (V); and RBC (VI). Cells were quantified 3 d after i.p. injection of PHZ, 50 mg/kg/d for 2 consecutive days. Two-tailed Student's *t* test. Results are presented as mean ± SEM ($n = 6$). (*C* and *D*) Representative FACS plots and quantification of BM erythroblast islands (EI). ns, not significant. Two-tailed Student's *t* test. Results are presented as mean ± SEM ($n = 6$). (*E*) Representative immunofluorescent images of EI costained with TER119 and F4/80 or CD169. (Scale bars, 20 μM.) (*F*) Enzyme-linked immunosorbent assay analysis of erythropoietin (EPO) in plasma of saline- or PHZ-treated *GCN2*$^{+/+}$ and *GCN2*$^{-/-}$ mice. ns, nonsignificant. Two-tailed Student's *t* test. Results are presented as mean ± SEM ($n = 3$–4). (*G*) Quantification of different BM Mφ populations in PHZ-treated *GCN2*$^{+/+}$ and *GCN2*$^{-/-}$ mice. The absolute number and frequency of the cells per femur were quantified 3 d after i.p. injection of PHZ, 50 mg/kg/d for 2 consecutive days. Two-tailed Student's *t* test. Results are presented as mean ± SEM ($n = 6$). *$P < 0.05$, **$P < 0.01$, ***$P < 0.001$.

both at the steady state and following hemolysis (Fig. 3*C*). Lack of iron storage appeared specifically in the *GCN2*$^{-/-}$ liver and not in the spleen (Fig. 3*C*). Diminished iron stores in *GCN2*$^{-/-}$ liver Mφ are presumably caused by the decreased efficiency of Mφ in ingesting RBCs and not by a lower number of Mφ, as the numbers of F4/80^{high} CD11b^{high} Mφ in FACS analysis were not different between *GCN2*$^{+/+}$ and *GCN2*$^{-/-}$ mice (Fig. 3*B*). F4/80 staining of liver sections also did not detect a significant difference between *GCN2*$^{+/+}$ and *GCN2*$^{-/-}$ livers (*SI Appendix*, Fig. S2*E*). This finding raises the possibility that during hemolysis, *GCN2*$^{-/-}$ liver Mφ are defective in RBC clearance and iron recycling.

Following phagocytosis of RBCs by Mφ, lysosomes fuse to phagosomes to form erythrophagolysosomes and start degradation of RBCs. Since our data show that *GCN2*$^{-/-}$ liver Mφ are defective in RBC clearance during stress, we surmised that erythrophagocytosis was impaired in these cells. We used electron microscopy (EM) analysis to visualize erythrophagocytic liver Mφ following hemolytic stress. EM images confirmed that PHZ treatment causes deformation of RBCs and the appearance of internal electron-dense spots (Heinz bodies) (42) (Fig. 3*D*, and *SI Appendix*, Fig. S3). Professional phagocytes form polymorphic immature lysosomes, which eventually transform into large round lysosomes and then small electron-dense mature lysosomes (Fig. 3D, and *SI Appendix*, Fig. S3) (43, 44). Quantification of the small electron-dense lysosomes (ranging between 0.5 and 0.6 μm in diameter) did not show a significant difference between PHZ-treated *GCN2*$^{+/+}$ and *GCN2*$^{-/-}$ liver Mφ (Fig. 3*E*). However, the number of large and polymorphic immature lysosomes (≥ 2 μm in diameter) was significantly higher in PHZ-treated *GCN2*$^{-/-}$ liver Mφ compared with *GCN2*$^{+/+}$ counterparts (Fig. 3*F*). To directly examine erythrophagocytosis in vitro, we exposed *GCN2*$^{+/+}$ and *GCN2*$^{-/-}$ BM-derived Mφ (BMDMs) to opsonized RBCs. The number of RBCs per BMDM was significantly higher in *GCN2*$^{+/+}$ BMDMs compared with *GCN2*$^{-/-}$ BMDM (*SI Appendix*, Fig. S2*F*). Together, our data suggest that lack of GCN2 impairs lysosome maturation, RBC clearance, and iron recycling by liver Mφ.

Regulation of Iron Homeostasis and Lysosomal Genes by GCN2-ATF4-NRF2 Pathway. To investigate the molecular mechanisms by which GCN2 regulates RBC clearance by Mφ, we assessed ATF4 targets by ChIP-sequencing (ChIP-seq) analysis (GSE166590). The ATF4 ChIP-seq analysis identified *Nfe2l1* (encoding NRF1) and *Nfe2l2* (encoding NRF2) as

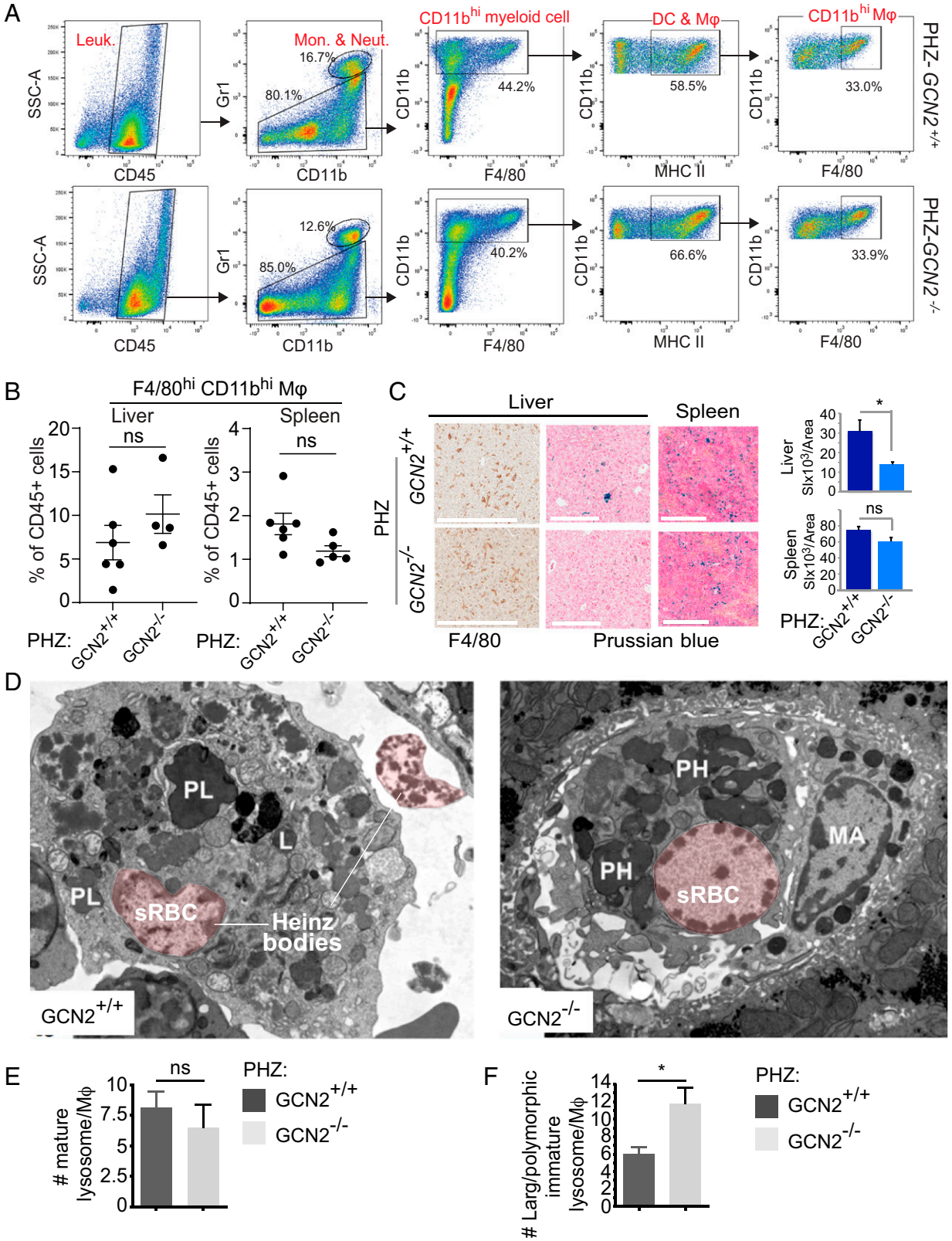

Fig. 3. Lack of GCN2 impairs erythrophagocytosis and iron recycling in liver macrophages during hemolysis. (*A*) Gating strategy of liver Mφ in PHZ-treated *GCN2*$^{+/+}$ and *GCN2*$^{-/-}$ mice for the analysis presented in 3*B* and *SI Appendix*, Fig. S2*D*. (*B*) Quantification of liver and spleen Mφ 3 d after i.p. injection of PHZ (50 mg/kg/d) for 2 consecutive days. ns., nonsignificant. Two-tailed Student's *t* test. Results are presented as mean ± SEM (n = 4–6). The gating strategy of spleen Mφ is shown in *SI Appendix*, Fig. S2*C*. (*C*) Representative images and quantification of Prussian blue staining of liver and spleen samples of *GCN2*$^{+/+}$ and *GCN2*$^{-/-}$ mice treated with PHZ as described in *B*. (Scale bar, 200 μM.) Representative images of F4/80 staining of the liver sections are presented in the *Left* panels. (Scale bar, 300 μM.) Quantifications of F4/80 staining are provided in *SI Appendix*, Fig. S2*E*. Two-tailed Student's *t* test. Results are presented as mean ± SEM (n = 5). (*D*) Representative EM images of *GCN2*$^{+/+}$ and *GCN2*$^{-/-}$ liver Mφ stained with uranyl acetate and lead citrate after PHZ treatment. A PHZ-treated *GCN2*$^{+/+}$ liver Mφ phagocytized a stressed RBC (sRBC) and exhibits different stages of lysosomal maturation from large immature lysosomes (PL) to mature lysosomes (L). Lysosomes of PHZ-treated *GCN2*$^{-/-}$ liver Mφ are polymorphic and immature (PH). MA, nonphagocytic Mφ. Heinz bodies are aggregates of irreversibly denatured Hgb attached to the RBC membrane that are caused by PHZ-mediated Hgb oxidation. (*E* and *F*) Quantification of mature (*E*) and large/polymorphic immature (*F*) lysosomes per liver Mφ in EM images. Two-tailed Student's *t* test. Results are presented as mean ± SEM. ns, not significant. *$P < 0.05$.

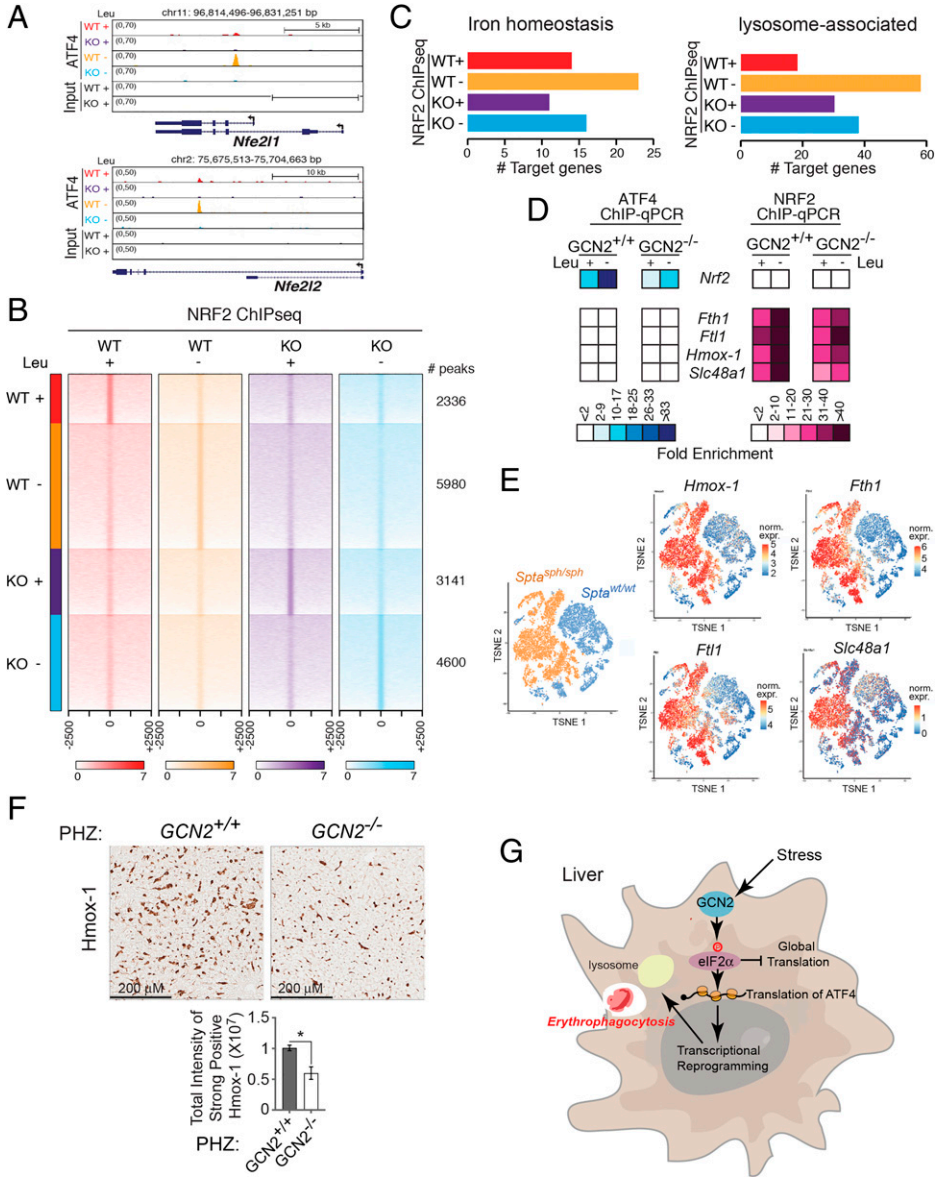

Fig. 4. GCN2-ATF4-NRF2 pathway controls genes involved in RBC clearance and iron recycling. (*A*) *Nfe2l1* (encoding Nrf1) and *Nfe2l2* (encoding Nrf2) genomic loci are bound by ATF4 identified by ChIP-seq analysis in $GCN2^{+/+}$ (WT) and $GCN2^{-/-}$ (KO) MEFs ± leucine (Leu) for 24 h. (*B*) Heatmap of NRF2 ChIP-seq binding peak signal intensities in a window of ±2.5 kb from peak center (0) identified in WT and KO MEFs ± Leu for 24 h. (*C*) NRF2 recruitment to genes involved in iron homeostasis and lysosome function. (*D*) ATF4 and NRF2 ChIP-qPCR analysis of a subset of NRF2 targets involved in iron homeostasis in $GCN2^{+/+}$ and $GCN2^{-/-}$ MEFs ± Leu for 24 h. (*E*) t-distributed stochastic neighbor embedding (t-SNE) plot visualization of scRNA-seq data of liver Mφ reported by Pfefferlé et al. (54). The expression of *Hmox1*, *Fth1*, *Ftl1*, and *Slc48a1* is presented in global t-SNE plots. Statistical analysis of differential gene expression is presented in *SI Appendix*, Dataset S1. (*F*) Representative images and quantification of Hmox-1 immunohistochemistry staining of liver sections from $GCN2^{+/+}$ and $GCN2^{-/-}$ mice, 3 d after i.p. injection of PHZ (50 mg/kg/d) for 2 consecutive days. Two-tailed Student's *t* test. Results are presented as mean ± SEM (n = 3). $*P < 0.05$ (Scale bars, 200 μm.) (*G*) A model summarizing the role of GCN2 in regulating erythrophagocytosis via liver Mφ.

GCN2-dependent targets of ATF4 (Fig. 4*A*). This result is consistent with a recent report of transcriptional control of NRF2 via the PERK-ATF4 pathway (45). NRF2 (*NFE2L2*, nuclear factor [erythroid-derived 2]-like 2) is a transcription factor that in addition to its well-characterized function in oxidative stress and toxicity, plays a critical role in iron homeostasis, heme biosynthesis, and Mφ inflammatory response (46–48). Importantly, NRF2 is involved in the recruitment of iron-recycling Mφ to the liver during hemolysis and stress erythropoiesis (26, 49). To determine whether the activity of NRF2 is controlled by GCN2, we performed ChIP-seq analysis of NRF2 in $GCN2^{+/+}$ (WT) and $GCN2^{-/-}$ (KO) mouse embryonic fibroblasts (MEFs) in the presence or absence of L-leucine for 24 h. De novo motif analysis identified enrichment of the NRF2 antioxidant response element in the peak summits (*SI Appendix*, Fig. S4*A*), and NRF2 binding sites were predominantly located at the genomic loci of coding genes (exons or introns) (*SI Appendix*, Fig. S4*B*).

ChIP-seq results demonstrated that L-leucine deficiency significantly increased the number of NRF2 binding sites in WT cells (from 2,336 in the presence of L-leucine to 5,980 in the absence of L-leucine) and that this increase was largely blocked by the lack of GCN2 (Fig. 4*B*). Among NRF2 target genes, several have been implicated in iron homeostasis and lysosome function (Fig. 4*C*). ChIP-qPCR confirmed that the binding of ATF4 to *Nfe2l2* and the recruitment of NRF2 to iron regulatory targets (*Hmox-1* [heme oxygenase 1], *FTH1* [ferritin heavy chain 1], *FTL1* [ferritin light chain 1], and *SLC48A1* [HRG1, heme-responsive gene1]) are dependent on GCN2 activity since the deletion of GCN2 largely blocked the stimulatory effect of L-leucine deprivation on ATF4 and NRF2 occupancy (Fig. 4*D*). *SLC48A1*,

Hmox1, *Fth1*, and *Ftl1* work together to carry out critical steps in iron recycling (*SI Appendix*, Fig. S4*C*) (41). SLC48A1 is a lysosomal membrane-bound transporter that exports heme out of lysosomes after RBCs are degraded in phagolysosomes (50, 51). Hmox-1 catalyzes heme into carbon monoxide, ferrous iron, and biliverdin/bilirubin (52). The released iron from the heme is either stored bound to ferritin or exported to circulation by ferroportin. FTH1 and FTL1 constitute the heavy and light subunits of ferritin, the major intracellular complex of iron storage (53). Importantly, single-cell RNA sequencing (scRNA-seq) analysis of liver Mφ revealed enrichment of the NRF2 signaling pathway in erythrophagocytic Mφ[54]. Supporting our model, reanalyzing the data from a model of inborn hemolytic anemia deposited by Pfefferlé et al. (54) revealed that the expression of several GCN2-dependent NRF2 targets (*Hmox1*, *FTH1*, *FTL1*, and *SLC48A1*) is specifically induced in erythrophagocytic liver Mφ ($Spta^{sph/sph}$) (Fig. 4*E*). It has been demonstrated that erythrophagocytosis by $Hri^{-/-}$ Mφ is impaired in vivo under chronic hemolytic anemia induced by the low level of PHZ treatment (55). Therefore, in addition to GCN2, HRI may contribute to the induction of NRF2 targets in erythrophagocytic liver Mφ. Collectively, these results demonstrate that regulation of the ATF4-NRF2 axis by GCN2 drives the expression of liver Mφ genes that are critical for RBC clearance and iron recycling.

Hmox-1 Is a Major Target of NRF2 Downstream of the GCN2-ATF4 Pathway. Next, we focused on Hmox-1 because of its known critical role in stress erythropoiesis and erythrophagocytosis (56, 57). *Hmox-1* knockout mice develop microcytic anemia and exhibit a defect in iron metabolism due to depletion of functional erythrophagocytic Mφ in the liver and spleen (58, 59). Consistent with GCN2-dependent activation of Hmox-1, PHZ-treated $GCN2^{-/-}$ mice display a lower level of total bilirubin in serum compared with their $GCN2^{+/+}$ counterparts (*SI Appendix*, Table S2). In support of our NRF2 ChIP-seq data, the stimulatory effect of L-leucine deprivation on Hmox-1 expression was significantly reduced in $GCN2^{-/-}$ and phospho-resistant eIF2 mutant (S51A) BMDMs (*SI Appendix*, Fig. S4 *D* and *E*). Similar results were observed in $GCN2^{-/-}$ MEFs and human dermal fibroblasts in which the expression of GCN2 was suppressed using short hairpin RNA (*SI Appendix*, Fig. S4 *F* and *G*). Immunostaining of liver sections also demonstrated that GCN2 loss suppresses the expression of Hmox-1 in hemolytic mice (Fig. 4*F*). Thus, these results suggest that GCN2 activity regulates the NRF2/Hmox-1 pathway.

Regulation of Genes Involved in Lysosome Maturation and Function by GCN2. ATF4 has been identified as a heterodimerization partner of NRF2 for the regulation of a subset of genes (60). Interrogation of our ATF4 and NRF2 ChIP-seq data in $GCN2^{+/+}$ and $GCN2^{-/-}$ cells identified targets cobound by both ATF4 and NRF2, several of which are involved in lysosome maturation and function (*SI Appendix*, Fig. S4*H*). Importantly, lysosomal acidity plays a key role in maintaining iron homeostasis (61). The acidification of lysosomes is mediated by vacuolar-type ATPase (v-ATPase) proton pump activity (62). We identified an essential component of v-ATPase, *ATP6v1f*, cotargeted by ATF4 and NRF2 under L-leucine deprivation (*SI Appendix*, Fig. S4*H*). We used LysoTracker Red to monitor lysosomal acidification in $GCN2^{+/+}$ and $GCN2^{-/-}$ BMDMs. As expected, BMDM exposure to lipopolysaccharide (LPS) increased the area of LysoTracker fluorescence present in $GCN2^{+/+}$ BMDMs; however, this effect was blunted in the absence of GCN2 (*SI Appendix*, Fig. S4 *I* and *J*). Thus, our data indicate that in addition to the NRF2 iron regulatory targets, GCN2-dependent control of lysosomal acidification may contribute to the defect in RBC clearance and iron recycling observed in $GCN2^{-/-}$ Mφ.

Discussion

Mφ have an intimate relationship with erythroid cells, starting with erythrocyte maturation within erythroblastic islands to erythrophagocytosis by specialized tissue-resident Mφ. Here, we described GCN2 as a regulator of erythrophagocytosis during stress conditions. Our data show that GCN2 promotes liver Mφ to dispose of damaged RBCs and recycle iron. EM analysis of liver Mφ revealed impaired maturation of lysosomal vesicles in $GCN2^{-/-}$ mice. This is consistent with a recent report that demonstrated that in response to amino acid deprivation, GCN2 controls the expression of lysosomal genes such as hydrolases (63). Importantly, NRF2 ChIP-seq analysis in $GCN2^{+/+}$ and $GCN2^{-/-}$ cells demonstrated that GCN2 regulates several NRF2 targets that are involved in iron recycling and lysosomal function.

While we chose to focus our study on the role of GCN2 in regulating Mφ in stress erythrophagocytosis, a large body of work has also established the role of HRI-eIF2α-ATF4 in regulating RBC life cycle (9). HRI is highly expressed in the erythroid lineages and coordinates globin synthesis with heme availability. Lack of HRI in the presence of iron deficiency or β-thalassemia inhibits erythroid differentiation. Iron deficiency similarly blocks erythroid differentiation in erythroid-specific $eIF2\alpha^{A/A}$ knock-in and $ATF4^{-/-}$ mice (64, 65). HRI is also required for Mφ maturation and erythrophagocytosis (55). Therefore, at least two members of eIF2AKs play a critical role in regulating RBC life cycle during stress conditions, GCN2 mainly through regulating tissue-resident Mφ and HRI primarily through regulating erythroid lineages. Our study links the activity of GCN2-eIF2α-ATF4 to iron metabolism in mammals. Studies in *Saccharomyces cerevisiae* have demonstrated that iron deficiency suppresses global translation through activation of the Gcn2-eIF2α pathway (66), and Gcn2-eIF2α-Gcn4 axis activation up-regulates the expression of genes required for iron uptake to promote intracellular iron content (67). Collectively, these studies connect a highly conserved amino acid sensing pathway to the RBC life cycle and iron metabolism, and suggest that modulation of GCN2 activity may be an important regulatory node in the control of RBC-related disorders. Interestingly, previous studies demonstrated that the production of Hgb in response to leucine deficiency is mediated via mTORC1/4E-BP and not GCN2 or HRI (68). Future studies will assess the role of GCN2 in RBC production.

Materials and Methods

Stress Treatments. For hemolytic anemia induction, mice received an i.p. injection with 50 mg/kg body weight PHZ (Sigma-Aldrich, P26252) or sterile saline on days 0 and 1 of the experiment. LDD (Research Diets, Inc.) mice were fed for 7 d. Finally, mice were exposed to chronic hypoxia (10% O_2) for 9 d in a special ventilated chamber in which normobaric hypoxia was established by diluting ambient air with nitrogen. The injection of N_2 gas inside the chamber was controlled by solenoid valves (OxyCycler model A84XOV, BioSpherix) automatically operated by the AnaWin 2 software.

Flow Cytometry and Cell Sorting. Flow cytometric analyses were carried out in single-cell suspensions of nucleated cells enriched from the spleen, liver, or flushed BM using an LSR Fortessa flow cytometer (BD Biosciences). Cell sorting experiments were performed using a MoFlo Astrios EQ Cell Sorter (Beckman

Coulter). Dead cells and debris were excluded by forward scatter (FSC), side scatter (SSC), and DAPI (4′,6-diamino-2-phenylindole) staining profiles. Spleen and liver were digested with collagenase type IV and DNase I (Roche) in a shaking incubator (37 °C) with 250 rpm for 15–30 min; then cells were filtered by 70 μm nylon cell strainers (Falcon). RBCs within flushed BM and spleen were lysed by lysis buffer (BD Biosciences) in accordance with the manufacturer's instructions. For erythroblast analysis, BM cells from femurs and tibia were flushed into 1x phosphate-buffered saline (PBS) with 0.1% bovine serum albumin (BSA). $CD45^+$ cells in BM were removed by CD45 antibody-labeled Dynabeads (Invitrogen, #11035). Then 2×10^6 $CD45^-$ cells were blocked with antimouse CD16/32 antibody and subsequently stained with fluorescein isothiocyanate (FITC)-conjugated antimouse CD45, CD11b, Gr-1, Alex Fluor 700-conjugated anti-Ter119, and Percep-Cy5.5-conjugated CD44 antibodies on ice for 30 min. DAPI was used to exclude dead cells.

To collect leukocyte populations, including Mφ in liver, liver cells were resuspended with 40% Percoll for density gradient centrifugation with 2,000 × g at 20 °C for 20 min without any break/accelerations. Single-cell populations collected from BM, liver, and spleen were maintained on ice for staining with flow cytometry antibodies. Liver and spleen Mφ were stained with CD45, CD11b, F4/80, and MHC II antibodies and Gr1 antibody was used to exclude monocytes and neutrophils. For BM analyses, femurs were flushed gently with 1 mL of ice-cold PEB (PBS/2 mM EDTA/0.5% BSA) buffer through a 1 mL syringe with a 21 gauge (G) needle into FACS tubes and processed for staining. BM erythroblast island quantification was described previously (24). Briefly, BM was flushed gently with Iscove modified Dulbecco medium (Gibco) containing 3.5% sodium citrate and 20% fetal calf serum solution using an 18 G syringe. Cells were then stained and diluted in FACS buffer containing DAPI without centrifugation or disruption until processed for the F4/80+ Ter119+ CD169+ multiplet population. Flow data were collected using a Fortessa LSRII analyzer, and data analysis was performed with FlowJo software (Tree Star; FlowJo™ v10.8 Software (BD Life Sciences) for Windows) or FACSDiva software (BD Biosciences; BD FACSDiva software, Becton, Dickinson and Company).

Complete Blood Count Analysis and Serum Biochemical Indices. Blood was harvested by retro-orbital sampling of mice anesthetized with isoflurane or following cardiac puncture and collected in polypropylene tubes containing EDTA. Blood parameters were measured with either scil Vet ABC Plus, Horiba, or Advia 120 Hematology System (Siemens). For serum biochemistry, blood samples were centrifuged at 3,600 rpm for 8 min, and sera were separated for analysis with Vitros 250, Ortho Clinical Diagnostics, at The Comparative Medicine and Animal Resources Centre, McGill University.

Quantification of Mouse EPO by Enzyme-Linked Immunosorbent Assay. Whole blood samples were collected by retro-orbital puncture into capillary blood collection tubes containing EDTA (BD Microtainer, BD 365974). Blood samples were centrifuged at 2,000 × g, 4 °C for 15 min. The resulting supernatant (plasma) was transferred to prechilled microcentrifuge tubes and placed on ice. A mouse EPO immunoassay was then performed using Invitrogen Mouse EPO ELISA Kit (EM28RB, Invitrogen) according to product instructions. Absorbance was measured using a FlexStation 3 Microplate Reader (Molecular Devices, LLC, San Jose, CA) at 450 nm. Each sample was measured in triplicate, and a standard curve was generated to quantify EPO concentration (pg/mL) for each sample. Mean plasma EPO (pg/mL) was calculated and plotted for saline- and PHZ-treated mice.

Quantification of Serum Iron, TIBC, and UIBC. Serum iron, TIBC, and UIBC concentrations were measured using the Iron/TIBC Reagent Set (Catalog Number, I750460, Pointe Scientific Inc, Canton, MI). The assays were performed according to the provided kit instructions but were scaled down linearly (by a factor of 20) to minimize sample use (25 μL) and allow the assays to be performed on 96 well plates. Pipettes and tubes were made iron free by washing with hot, (1:2) hydrochloric solution and rinsing several times with iron-free distilled water. Absorbance was measured using a FlexStation 3 Microplate Reader (Molecular Devices, LLC) at 560 nm twice during the experiment. Iron concentrations (μg/dL) were calculated per protocol instructions. The UIBC was measured based on the difference between the amount of ferrous ions added and the unbound ions. The value for UIBC was used for calculating TIBC according to manufacturer instructions.

ChIP-qPCR and ChIP-seq. ChIP-qPCR and ChIP-seq experiments were performed using WT and KO mice MEFs ± leucine deprivation (DMEM - leucine (Crystalgen), 10% Dialyzed FBS One Shot (gibco; REF A33820-01)) for 24 h. Cells were crosslinked with 1% formaldehyde at room temperature for 10 min. Crosslinking was quenched by the addition of quenching buffer (1 M glycine buffer, 125 mM as a final concentration) and incubated at room temperature for 5 min with gentle agitation. Crosslinked cells were lysed, and resuspended nuclei were sonicated. For each ChIP, 5 μg of either anti-ATF4 (sc-200, Santa-Cruz) or anti-NRF2 (ab62352, Abcam) were immobilized overnight at 4 °C on 50 μL Protein G Dynabeads (Cat#10004D, Thermo Fisher) diluted in 500 ul of PBS + 0.5% bovine serum albumin (BSA). The next day, the antibody-conjugated beads were washed twice with PBS + 0.5% BSA. Sonicated chromatin (75 μg) was diluted in 2.5X ChIP dilution buffer (Tris 20 mM, ph 8, NaCl 100 nM, EDTA 2 mM, pH 8, Triton-X-100 0.5%) + 100 μL of PBS + 0.5% BSA and added to the antibody-bound beads and left to rotate overnight at 4 °C. Then, the beads were washed 3X with 1 mL LiCl wash buffer (Tris 100 nm, LiCl 500 nM, Na-desoxycholate 1%, Nonidet P-40 1%), transferred to new tubes, then washed 2X more with LiCl wash buffer followed by a quick wash with Tris-EDTA (TE) buffer. DNA was eluted with 300 μL decrosslink buffer ($NaHCO_3$ 0.1 M, sodium dodecyl sulfate (SDS) 1%) overnight at 65 °C. RNase A (0.2 ug/ul final) was added to the samples and left at 37 °C for 1 h followed by addition of Proteinase K (0.2 ug/ul final) and incubation at 55 °C for 30 min. ChIP DNA was purified using a QIAquick PCR purification kit (Qiagen). For ChIP-qPCR, fold enrichments were normalized to the binding to two nonbound control regions.

For NRF2 ChIP-seq, DNA libraries and sequencing were performed at the Génome Québec Innovation Centre. DNA library preparation was done using the TruSeq DNA sample preparation kit (FC-121-2003; Illumina) according to Illumina recommendations. The ChIP DNA libraries were sequenced as single 50 bp reads (tags) using an Ilumina HisEq. 2500 sequencer (Illumina). Raw reads were trimmed for length ($n \geq 50$), quality (phred score ≥ 30) and adapter sequence using Fastx v0.0.13.2 (FASTQ/A short-reads pre-processing tools, http://hannonlab.cshl.edu/fastx_toolkit/). Trimmed reads were then aligned to the mouse reference genome mm10 using BWA v0.7.12 (69). Peaks were called using MACS (Model-based Analysis of ChIP-Seq) v2.1.0 software and default parameters (mfold = [5,50]; FDR cutoff = 0.05, –nomodel) using sequenced libraries of either WT or GCN2 KO input DNA as control (70). The regions defined by the peak summit ±150 bp were used for downstream analysis. Peak annotations, tag directory, bed files, and de novo motif discovery were performed using HOMER (Hypergeometric Optimization of Motif EnRichment) v4.7 (71). For peak intersections, peak list intersections were performed using the R package GenomicRanges v1.26.4 (72). Binding peaks were considered overlapping if their peak summits were within 300 bp or less apart. Binding intensity heatmaps and tag density plots were produced by the R package Genomation v1.9.3 (73) with an estimated fragment length of 200 bp.

Statistical Analysis. For statistical comparison between two groups, unpaired, a two-tailed *t* test was used. For statistical comparison between more than two groups, ANOVA (Bonferroni correction) and post hoc tests were performed to identify the different means. Statistical analyses were performed with GraphPad Prism (version 9.0.0 for Windows, GraphPad Software, SanDiogo, California USA, www.graphpad.com). For differential analysis of gene expression of scRNA-seq data, normalized gene expression data were obtained from data previously deposited in the Gene Expression Ominibus database under accession ID GSE145241 (54). The file GSE145241_sce-SPTAmerged-Final.rds.gz was downloaded and analyzed using Seurat v3.0.1 in R (74). Differentially expressed genes for each sample type were determined using the FileAllMakers function using both the receiver operating characteristic (ROC) and Wilcoxon tests (SI Appendix, Dataset S1) (75). Significance was determined by either an area under the curve value greater than 0.8 for the ROC test or an adjusted *P* value less than 0.05 for the Wilcoxon test.

Data, Materials, and Software Availability. NRF2 ChIP-seq data have been deposited into the Gene Expression Omnibus database, accession number: GSE188460 (76). ATF4 ChIP-seq data are available under accession code GSE166590 (77). All other study data are included in the article and/or in *SI Appendix*.

ACKNOWLEDGMENTS. This work was funded by the Chicago Biomedical Consortium with support from the Searle Funds at The Chicago Community Trust and NIH 1R01HL163806-01 awarded to S.T. and by the Foundation grant from Canadian Institutes of Health Research, FND-148423, awarded to N.S. S.P. is funded by an NIH R01HL162584 award. This research was also supported by an NIH Pre-Doctoral Fellowship in the T32 Training Program in Lung Biology and Pathobiology (2T32HL007829-27) awarded to P.T. and T32HL007820 awarded to C.E.A., and NIH R01DK126753 awarded to K.-W.K. We thank George E. Chlipala, (Research Informatics Core, Research Resources Center, University of Illinois at Chicago) for analyzing single-cell RNA sequencing data. George E. Chlipala is supported in part by National Center for Advancing Translational Sciences through Grant UL1TR002003. We also thank Eloi Mercier and Guillaume Bourque (Canadian Centre for Computational Genomics, McGill University) for processing the raw ChIP-sequencing data, including alignment of reads, peak annotations, and heatmaps. Phosphoresistant eukaryotic initiation factor-2 mutant (S51A) bone marrow-derived macrophages were a generous gift from Jaeseok Han (Soonchunhyang University).

Author affiliations: [a]Department of Pharmacology and Regenerative Medicine, University of Illinois College of Medicine, Chicago, IL, 60612; [b]Department of Biochemistry, McGill University, Montreal, QC, H3A 1A3, Canada; [c]Rosalind and Morris Goodman Cancer Institute, McGill University, Montreal, QC, H3A 1A3, Canada; [d]Lady Davis Institute for Medical Research, Jewish General Hospital and Department of Medicine, McGill University, Montreal, QC, H3T 1E2, Canada; [e]Department of Anesthesia and Faculty of Dentistry, McGill University, Montreal, QC, H3A 0G1, Canada; [f]Department of Internal Medicine II, Medical University of Innsbruck, Innsbruck, 6020, Austria; [g]Department of Anatomy and Cell Biology, McGill University, Montreal, QC, H3G 1Y6, Canada; and [h]Nutrition and Microbiome Laboratory, Centre de recherche du CHUM and Department of Medicine, Université de Montréal, Montréal, QC, H3X 0A9, Canada

1. Y. Liu, A. Beyer, R. Aebersold, On the dependency of cellular protein levels on mRNA abundance. *Cell* **165**, 535–550 (2016).
2. M. Costa-Mattioli, P. Walter, The integrated stress response: From mechanism to disease. *Science* **368**, eaat5314 (2020).
3. A. G. Hinnebusch, I. P. Ivanov, N. Sonenberg, Translational control by 5′-untranslated regions of eukaryotic mRNAs. *Science* **352**, 1413–1416 (2016).
4. M. Dey *et al.*, PKR and GCN2 kinases and guanine nucleotide exchange factor eukaryotic translation initiation factor 2B (eIF2B) recognize overlapping surfaces on eIF2alpha. *Mol. Cell. Biol.* **25**, 3063–3075 (2005).
5. A. G. Hinnebusch, K. Natarajan, Gcn4p, a master regulator of gene expression, is controlled at multiple levels by diverse signals of starvation and stress. *Eukaryot. Cell* **1**, 22–32 (2002).
6. K. M. Vattem, R. C. Wek, Reinitiation involving upstream ORFs regulates ATF4 mRNA translation in mammalian cells. *Proc. Natl. Acad. Sci. U.S.A.* **101**, 11269–11274 (2004).
7. H. P. Harding *et al.*, Diabetes mellitus and exocrine pancreatic dysfunction in perk-/- mice reveals a role for translational control in secretory cell survival. *Mol. Cell* **7**, 1153–1163 (2001).
8. W. Lin *et al.*, The integrated stress response prevents demyelination by protecting oligodendrocytes against immune-mediated damage. *J. Clin. Invest.* **117**, 448–456 (2007).
9. J. J. Chen, S. Zhang, Heme-regulated eIF2α kinase in erythropoiesis and hemoglobinopathies. *Blood* **134**, 1697–1707 (2019).
10. S. Gal-Ben-Ari, I. Barrera, M. Ehrlich, K. Rosenblum, PKR: A kinase to remember. *Front. Mol. Neurosci.* **11**, 480 (2019).
11. B. A. Castilho *et al.*, Keeping the eIF2 alpha kinase Gcn2 in check. *Biochim. Biophys. Acta* **1843**, 1948–1968 (2014).
12. S. A. Wek, S. Zhu, R. C. Wek, The histidyl-tRNA synthetase-related sequence in the eIF-2 alpha protein kinase GCN2 interacts with tRNA and is required for activation in response to starvation for different amino acids. *Mol. Cell. Biol.* **15**, 4497–4506 (1995).
13. J. Deng *et al.*, Activation of GCN2 in UV-irradiated cells inhibits translation. *Curr. Biol.* **12**, 1279–1286 (2002).
14. H. Y. Jiang, R. C. Wek, Phosphorylation of the alpha-subunit of the eukaryotic initiation factor-2 (eIF2alpha) reduces protein synthesis and enhances apoptosis in response to proteasome inhibition. *J. Biol. Chem.* **280**, 14189–14202 (2005).
15. J. J. Berlanga *et al.*, Antiviral effect of the mammalian translation initiation factor 2alpha kinase GCN2 against RNA viruses. *EMBO J.* **25**, 1730–1740 (2006).
16. C. C. Wu, A. Peterson, B. Zinshteyn, S. Regot, R. Green, Ribosome collisions trigger general stress responses to regulate cell fate. *Cell* **182**, 404–416.e14 (2020).
17. M. Costa-Mattioli *et al.*, Translational control of hippocampal synaptic plasticity and memory by the eIF2alpha kinase GCN2. *Nature* **436**, 1166–1173 (2005).
18. R. Ravindran *et al.*, The amino acid sensor GCN2 controls gut inflammation by inhibiting inflammasome activation. *Nature* **531**, 523–527 (2016).
19. F. Guo, D. R. Cavener, The GCN2 eIF2alpha kinase regulates fatty-acid homeostasis in the liver during deprivation of an essential amino acid. *Cell Metab.* **5**, 103–114 (2007).
20. S. Won *et al.*, Increased susceptibility to DNA virus infection in mice with a GCN2 mutation. *J. Virol.* **86**, 1802–1808 (2012).
21. R. Ravindran *et al.*, Vaccine activation of the nutrient sensor GCN2 in dendritic cells enhances antigen presentation. *Science* **343**, 313–317 (2014).
22. K. Chaudhary *et al.*, Amino acid metabolism inhibits antibody-driven kidney injury by inducing autophagy. *J. Immunol.* **194**, 5713–5724 (2015).
23. D. Z. de Back, E. B. Kostova, M. van Kraaij, T. K. van den Berg, R. van Bruggen, Of macrophages and red blood cells; a complex love story. *Front. Physiol.* **5**, 9 (2014).
24. A. Chow *et al.*, CD169^{+} macrophages provide a niche promoting erythropoiesis under homeostasis and stress. *Nat. Med.* **19**, 429–436 (2013).
25. P. Ramos *et al.*, Macrophages support pathological erythropoiesis in polycythemia vera and β-thalassemia. *Nat. Med.* **19**, 437–445 (2013).
26. I. Theurl *et al.*, On-demand erythrocyte disposal and iron recycling requires transient macrophages in the liver. *Nat. Med.* **22**, 945–951 (2016).
27. M. Bessis, [Erythroblastic island, functional unity of bone marrow]. *Rev. Hematol. (Paris)* **13**, 8–11 (1958).
28. N. Mohandas, M. Prenant, Three-dimensional model of bone marrow. *Blood* **51**, 633–643 (1978).
29. M. Socolovsky, Exploring the erythroblastic island. *Nat. Med.* **19**, 399–401 (2013).
30. M. W. Hentze, M. U. Muckenthaler, B. Galy, C. Camaschella, Two to tango: Regulation of Mammalian iron metabolism. *Cell* **142**, 24–38 (2010).
31. M. P. Soares, I. Hamza, Macrophages and iron metabolism. *Immunity* **44**, 492–504 (2016).
32. M. J. Halaby *et al.*, GCN2 drives macrophage and MDSC function and immunosuppression in the tumor microenvironment. *Sci. Immunol.* **4**, eaax8189 (2019).
33. N. Tabatabaei, S. Hou, K. W. Kim, S. Tahmasebi, Signaling pathways that control mRNA translation initiation in macrophages. *Cell. Signal.* **73**, 109700 (2020).
34. M. Haldar *et al.*, Heme-mediated SPI-C induction promotes monocyte differentiation into iron-recycling macrophages. *Cell* **156**, 1223–1234 (2014).
35. B. D. Goldstein, M. G. Rozen, R. L. Kunis, Role of red cell membrane lipid peroxidation in hemolysis due to phenylhydrazine. *Biochem. Pharmacol.* **29**, 1355–1359 (1980).
36. A. Kornberg, Amino acids in the production of granulocytes in rats. *Fed. Proc.* **5**, 142 (1946).
37. A. Kornberg, F. S. Daft, W. H. Sebrell, Granulocytopenia and anemia in rats fed diets of low casein content. *Science* **103**, 646–648 (1946).
38. Y. Taya *et al.*, Depleting dietary valine permits nonmyeloablative mouse hematopoietic stem cell transplantation. *Science* **354**, 1152–1155 (2016).
39. M. Koulnis, Y. Liu, K. Hallstrom, M. Socolovsky, Negative autoregulation by Fas stabilizes adult erythropoiesis and accelerates its stress response. *PLoS One* **6**, e21192 (2011).
40. M. J. Koury, M. C. Bondurant, Erythropoietin retards DNA breakdown and prevents programmed death in erythroid progenitor cells. *Science* **248**, 378–381 (1990).
41. M. U. Muckenthaler, S. Rivella, M. W. Hentze, B. Galy, A red carpet for iron metabolism. *Cell* **168**, 344–361 (2017).
42. J. H. Jandl, L. K. Engle, D. W. Allen, Oxidative hemolysis and precipitation of hemoglobin. I. Heinz body anemias as an acceleration of red cell aging. *J. Clin. Invest.* **39**, 1818–1836 (1960).
43. C. Morales, Y. Clermont, L. Hermo, Nature and function of endocytosis in Sertoli cells of the rat. *Am. J. Anat.* **173**, 203–217 (1985).
44. B. Smedsrød *et al.*, Cell biology of liver endothelial and Kupffer cells. *Gut* **35**, 1509–1516 (1994).
45. C. Sarcinelli *et al.*, ATF4-dependent *NRF2* transcriptional regulation promotes antioxidant protection during endoplasmic reticulum stress. *Cancers (Basel)* **12**, E569 (2020).
46. Y. Chen *et al.*, Activation of Nrf2 attenuates pulmonary vascular remodeling via inhibiting endothelial-to-mesenchymal transition: An insight from a plant polyphenol. *Int. J. Biol. Sci.* **13**, 1067–1081 (2017).
47. E. H. Kobayashi *et al.*, Nrf2 suppresses macrophage inflammatory response by blocking proinflammatory cytokine transcription. *Nat. Commun.* **7**, 11624 (2016).
48. M. J. Kerins, A. Ooi, The roles of NRF2 in modulating cellular iron homeostasis. *Antioxid. Redox Signal.* **29**, 1756–1773 (2018).
49. O. T. Gbotosho *et al.*, Nrf2 deficiency in mice attenuates erythropoietic stress-related macrophage hypercellularity. *Exp. Hematol.* **84**, 19–28.e4 (2020).
50. A. Rajagopal *et al.*, Haem homeostasis is regulated by the conserved and concerted functions of HRG-1 proteins. *Nature* **453**, 1127–1131 10.1038/nature06934. (2008).
51. C. White *et al.*, HRG1 is essential for heme transport from the phagolysosome of macrophages during erythrophagocytosis. *Cell Metab.* **17**, 261–270 (2013).
52. G. Kovtunovych *et al.*, Wild-type macrophages reverse disease in heme oxygenase 1-deficient mice. *Blood* **124**, 1522–1530 (2014).
53. S. C. Andrews, The Ferritin-like superfamily: Evolution of the biological iron storeman from a rubrerythrin-like ancestor. *Biochim. Biophys. Acta* **1800**, 691–705 (2010).
54. M. Pfefferlé *et al.*, Hemolysis transforms liver macrophages into antiinflammatory erythrophagocytes. *J. Clin. Invest.* **130**, 5576–5590 (2020).
55. S. Liu *et al.*, The function of heme-regulated eIF2alpha kinase in murine iron homeostasis and macrophage maturation. *J. Clin. Invest.* **117**, 3296–3305 (2007).
56. Y. A. Cao *et al.*, Heme oxygenase-1 deletion affects stress erythropoiesis. *PLoS One* **6**, e20634 (2011).
57. S. T. Fraser *et al.*, Heme oxygenase-1 deficiency alters erythroblastic island formation, steady-state erythropoiesis and red blood cell lifespan in mice. *Haematologica* **100**, 601–610 (2015).
58. K. D. Poss, S. Tonegawa, Heme oxygenase 1 is required for mammalian iron reutilization. *Proc. Natl. Acad. Sci. U.S.A.* **94**, 10919–10924 (1997).
59. G. Kovtunovych, M. A. Eckhaus, M. C. Ghosh, H. Ollivierre-Wilson, T. A. Rouault, Dysfunction of the heme recycling system in heme oxygenase 1-deficient mice: Effects on macrophage viability and tissue iron distribution. *Blood* **116**, 6054–6062 (2010).
60. C. H. He *et al.*, Identification of activating transcription factor 4 (ATF4) as an Nrf2-interacting protein. Implication for heme oxygenase-1 gene regulation. *J. Biol. Chem.* **276**, 20858–20865 (2001).
61. R. A. Weber *et al.*, Maintaining iron homeostasis is the key role of lysosomal acidity for cell proliferation. *Mol. Cell* **77**, 645–655.e7 (2020).
62. J. A. Mindell, Lysosomal acidification mechanisms. *Annu. Rev. Physiol.* **74**, 69–86 (2012).
63. M. Nofal *et al.*, GCN2 adapts protein synthesis to scavenging-dependent growth. *Cell Syst.* **13**, 158–172.e9 (2021).
64. S. Zhang *et al.*, HRI coordinates translation by eIF2αP and mTORC1 to mitigate ineffective erythropoiesis in mice during iron deficiency. *Blood* **131**, 450–461 (2018).
65. H. C. Masuoka, T. M. Townes, Targeted disruption of the activating transcription factor 4 gene results in severe fetal anemia in mice. *Blood* **99**, 736–745 (2002).
66. A. M. Romero, L. Ramos-Alonso, P. Alepuz, S. Puig, M. T. Martínez-Pastor, Global translational repression induced by iron deficiency in yeast depends on the Gcn2/eIF2α pathway. *Sci. Rep.* **10**, 233 (2020).
67. M. Caballero-Molada *et al.*, The Gcn2-eIF2α pathway connects iron and amino acid homeostasis in *Saccharomyces cerevisiae*. *Biochem. J.* **475**, 1523–1534 (2018).
68. J. Chung *et al.*, The mTORC1/4E-BP pathway coordinates hemoglobin production with L-leucine availability. *Sci. Signal.* **8**, ra34 (2015).

69. H. Li, R. Durbin, Fast and accurate long-read alignment with Burrows-Wheeler transform. *Bioinformatics* **26**, 589–595 (2010).
70. Y. Zhang *et al.*, Model-based analysis of ChIP-Seq (MACS). *Genome Biol.* **9**, R137 (2008).
71. S. Heinz *et al.*, Simple combinations of lineage-determining transcription factors prime cis-regulatory elements required for macrophage and B cell identities. *Mol. Cell* **38**, 576–589 (2010).
72. M. Lawrence *et al.*, Software for computing and annotating genomic ranges. *PLOS Comput. Biol.* **9**, e1003118 (2013).
73. A. Akalin, V. Franke, K. Vlahovíček, C. E. Mason, D. Schübeler, Genomation: A toolkit to summarize, annotate and visualize genomic intervals. *Bioinformatics* **31**, 1127–1129 (2015).
74. T. Stuart, *et al.*, Comprehensive integration of single-cell data. *Cell*. **177**, 1888–1902; e1821. (2019).
75. X. Zhang *et al.*, CellMarker: A manually curated resource of cell markers in human and mouse. *Nucleic Acids Res.* **47** (D1), D721–D728 (2019).
76. P. Toboz *et al.*, The amino acid sensor GCN2 controls red blood cell clearance and iron metabolism through regulation of liver macrophages. Gene Expression Omnibus. http://www.ncbi.nlm.nih.gov/geo/query/acc.cgi?acc=GSE188460. Deposited 9 November 2021.
77. P. Toboz *et al.*, The amino acid sensor GCN2 controls red blood cell clearance and iron metabolism through regulation of liver macrophages. Gene Expression Omnibus. http://www.ncbi.nlm.nih.gov/geo/query/acc.cgi?acc=GSE166590. Deposited. 10 February 2021.